

## References and Notes

- E. Roedder, Ed., *Fluid Inclusions*, vol. 12 of *Reviews in Mineralogy* (Mineralogical Society of America, Washington, DC, 1984).
- H. Bureau, F. Pineau, N. Metrich, M. Semet, M. Javoy, *Chem. Geol.* **147**, 115 (1998).
- A. Gioncada *et al.*, *Bull. Volcanol.* **60**, 286 (1998).
- D. Massare, N. Métrich, R. Clocchiatti, *Chem. Geol.* **183**, 87 (2002).
- A. V. Sobolev, L. V. Dmitriev, V. L. Barsukov, V. N. Nevsorov, A. B. Slutsky, in *Igneous Processes and Remote Sensing*, vol. 11 of *Proceedings of the Lunar and Planetary Science Conference*, P. R. Criswell, R. B. Merrill, Eds. (Pergamon, New York, 1980), pp. 105–116.
- P. Schiano, *Earth Sci. Rev.* **63**, 121 (2003).
- B. J. Wanmaker, B. Evans, *Contrib. Mineral. Petrol.* **102**, 102 (1989).
- D. B. Dingwell, K. U. Hess, C. Romano, *Earth Planet. Sci. Lett.* **158**, 31 (1998).
- Y. Zhang, Z. Xu, Y. Liu, *Am. Mineral.* **88**, 1741 (2003).
- W. A. Deer, R. A. Howie, J. Zussman, *Orthosilicates* (Longman, London, 1962).
- A. Baronnet, *Fortschr. Miner.* **62**, 187 (1984).
- L. C. Kuo, R. J. Kirkpatrick, *Am. J. Sci.* **285**, 51 (1985).
- C. H. Donaldson, *Lithos* **8**, 163 (1975).
- J. E. Mungall, C. Romano, D. B. Dingwell, *Am. Mineral.* **83**, 685 (1998).
- D. Snyder, E. Gier, I. Carmichael, *J. Geophys. Res.* **99**, 15503 (1994).
- D. R. Olander, A. J. Machiels, M. Balooch, S. K. Yagnik, *J. Appl. Phys.* **53**, 669 (1982).
- H. E. Cline, T. R. Anthony, *J. Appl. Phys.* **43**, 10 (1972).
- D. R. H. Jones, *J. Cryst. Growth* **20**, 145 (1973).
- W. A. Tiller, *The Science of Crystallization: Microscopic Interfacial Phenomena* (Cambridge Univ. Press, Cambridge, UK, 1991).
- G. Brandeis, C. Jaupart, C. J. Allègre, *J. Geophys. Res.* **89**, 10161 (1984).
- R. J. Kirkpatrick, in *Reviews in Mineralogy vol 8*, A. C. Lasaga, R. J. Kirkpatrick, Eds. (Mineralogical Society of America, Washington, DC, 1981), pp. 321–398.
- J. C. Mareschal, C. Jaupart, *Earth Planet. Sci. Lett.* **223**, 65 (2004).
- S. V. Sobolev *et al.*, *Tectonophysics* **275**, 143 (1997).
- N. M. Shapiro, M. H. Ritzwoller, J. C. Mareschal, C. Jaupart, in *Geological Prior Information: Informing Science and Engineering*, A. Curtis, R. Wood, Eds. (Geological Society of London Special Publication, London, 2004), vol. 239, pp. 175–194.
- P. Schiano, R. Clocchiatti, *Nature* **368**, 621 (1994).
- M. J. Cordery, J. P. Morgan, *J. Geophys. Res.* **98**, 19477 (1993).
- Y. J. Chen, J. Lin, *Earth Planet. Sci. Lett.* **221**, 263 (2004).
- C. G. Farnetani, B. Legras, P. J. Tackley, *Earth Planet. Sci. Lett.* **196**, 1 (2002).
- T. J. Henstock, *Geophys. Res. Lett.* **29**, 1137 (2002).
- J. Maumus, D. Laporte, P. Schiano, *Contrib. Mineral. Petrol.* **148**, 1 (2004).
- P. Schiano *et al.*, *Earth Planet. Sci. Lett.* **160**, 537 (1998).
- M. M. Hirschmann, M. B. Baker, E. M. Stolper, *Geochim. Cosmochim. Acta* **62**, 883 (1998).
- E. Aharonov, J. A. Whitehead, P. B. Kelemen, M. Spiegelman, *J. Geophys. Res.* **100**, 20433 (1995).
- We thank B. Thellier and D. Massare for technical assistance. Financial support was provided by the European Community's Human Potential Programme under contract HPRN-CT-2002-00211 (Euromelt).

## Supporting Online Material

www.sciencemag.org/cgi/content/full/314/5801/970/DC1

Figs. S1 and S2

Tables S1 and S2

Reference

13 July 2006; accepted 10 October 2006

10.1126/science.1132485

# Selective Etching of Metallic Carbon Nanotubes by Gas-Phase Reaction

Guangyu Zhang,\* Pengfei Qi,\* Xinran Wang, Yuerui Lu, Xiaolin Li, Ryan Tu, Sarunya Bangsaruntip, David Mann, Li Zhang, Hongjie Dai†

Metallic and semiconducting carbon nanotubes generally coexist in as-grown materials. We present a gas-phase plasma hydrocarbonation reaction to selectively etch and gasify metallic nanotubes, retaining the semiconducting nanotubes in near-pristine form. With this process, 100% of purely semiconducting nanotubes were obtained and connected in parallel for high-current transistors. The diameter- and metallicity-dependent “dry” chemical etching approach is scalable and compatible with existing semiconductor processing for future integrated circuits.

Carbon nanotubes have shown promise for future electronics (1–6). However, a major roadblock to the scaling up of single-walled carbon nanotube (SWNT) field-effect transistors (FETs) has been the difficulty in obtaining purely semiconducting SWNTs (S-SWNTs) without electrical short by metallic SWNTs (M-SWNTs). Parallel S-SWNTs are necessary to enable high-current and high-speed nanotube FETs to surpass modern silicon devices. Various approaches have been developed for selective synthesis of S-SWNTs (7, 8), electrical breakdown of M-SWNTs (9, 10), solution-phase chemical separation (11, 12) and selective chemical modification (13–15). For large-scale circuits, much remains to be

done to achieve full semiconductor yield, high scalability of metallic SWNT removal, optimum nanotube diameter and length, and highly preserved electrical properties of SWNTs.

Here, we demonstrate a methane plasma followed by an annealing process to selectively hydrocarbonate M-SWNTs and retain S-SWNTs grown on substrates. The retained S-SWNTs are free of covalent alterations, are stable at high temperatures, and exhibit electrical properties similar to pristine materials. The distribution of diameters of the S-SWNTs is narrowed down to a window (~1.3 to 1.6 nm) that provides sufficient band gaps for high on/off ratios and allows for good electrical contacts (16), both of which are important in high-performance electronics. The dual effects of selective metal removal and diameter distribution narrowing combined with compatibility with microfabrication technology make the method promising for large-scale SWNT electronics.

We first fabricated an array (Fig. 1A) of 98 “few-tube” electrical devices on SiO<sub>2</sub>(67 nm)/Si (as back-gate) (Fig. 1A, bottom) substrates, with each device comprising 0 to 3 as-grown SWNTs [by patterned chemical vapor deposition (CVD) growth (17) at 800°C] bridging source-drain (S-D) Ti/Au electrodes (S-D distance ~400 nm) (Fig. 1A). The particular CVD recipe produced SWNTs in a broad diameter (*d*) range of *d* = 1 to 2.8 nm, measured by atomic force microscopy (AFM). About 55% of the as-fabricated devices (out of 244 measured on six chips) were found to be “depletable” (D) by sweeping gate-voltage with on/off conductance ratios ≥10<sup>3</sup>. These were devices fortuitously composed of one or multiple (two or three) as-grown S-SWNTs. The other 45% of the devices contained at least one M-SWNT (with or without S-SWNT) and were “nondepletable” (ND) with on/off ratios ≤10.

We treated hundreds of as-made few-tube device arrays by exposure to a methane plasma at 400°C, followed by 600°C annealing in vacuum in a 4-inch quartz-tube furnace equipped with a remote plasma system (18). The use of methane plasma instead of hydrogen plasma was found key to selective M-SWNT etching because of milder reactivity and higher controllability. After the treatment, the percentage of depletable devices increased from ~55% (out of 244) to ~93% (out of 78 that survived), with only a few nondepletable devices remaining (Fig. 2A), indicating that selective removal of metallic SWNTs over semiconducting ones was occurring.

We observed five different behaviors with the 244 few-tube devices after the treatments, including ND→D (i.e., non-

Department of Chemistry and Laboratory for Advanced Materials, Stanford University, Stanford, CA 94305, USA.

\*These authors contributed equally to this work.

†To whom correspondence should be addressed. E-mail: hdai@stanford.edu

depletable became depletable,  $\sim 10\%$ ) (Fig. 1B); D $\rightarrow$ D (20% remained depletable) (Fig. 1C); ND $\rightarrow$ ND (2%) (Fig. 1D); ND $\rightarrow$ LOST (34% became electrically insulating (Fig. 1E); and D $\rightarrow$ LOST (34%) (Fig. 1F). In all ND $\rightarrow$ D devices, AFM revealed at least one (metallic) tube etched into pieces or nearly removed from the substrate and the existence of fully intact S-SWNTs (Fig. 1B, inset). Intact tubes were observed in ND $\rightarrow$ D and D $\rightarrow$ D devices (Fig. 1, B and C, insets), respectively, and etched tubes were observed in the LOST devices (Fig. 1, E and F, insets).

The semiconducting SWNTs in D $\rightarrow$ LOST devices (with only S-SWNTs) were “mis-killed” by the plasma treatment. Notably, we found that these devices when as-made all exhibited low on-state conductance ( $G < \sim 5 \mu\text{S}$ ) (Fig. 2B) and were composed of predominantly small-diameter S-SWNTs with  $d \leq 1.4 \text{ nm}$  (Fig. 2E), as revealed by AFM. The low on-conductance was consistent with small-diameter, large band gap ( $E_g \sim 1/d$ ), high Schottky barriers at the metal-tube contacts, and thus with high resistances (16). The surviving semiconductor D $\rightarrow$ D devices mostly exhibited higher conductance (Fig. 2C) and contained larger-diameter ( $d \geq 1.4 \text{ nm}$ ) tubes observed by AFM (Fig. 2G). These results showed that small-diameter S-SWNTs were selectively etched over large S-SWNTs. On the other hand, analysis of the ND $\rightarrow$ LOST devices (with M-SWNTs) found a wider span of conductance (Fig. 2D), with tube diameters mainly in the range of 1 to 2 nm (Fig. 2F). This suggested that metallic SWNTs with small and medium diameters ( $d < 2 \text{ nm}$ ) were all etched in the ND $\rightarrow$ LOST devices. For the few ND $\rightarrow$ ND devices remaining, we imaged all tubes in these devices and always observed the existence of large tubes ( $d > \sim 2 \text{ nm}$ ) (Fig. 2H and Fig. 1D, inset), suggesting that large metallic tubes could survive the plasma. Taken together, our data revealed that in the small-diameter regime ( $d \leq 1.4 \text{ nm}$ ), M- and S-SWNTs were etched nondiscriminately (Fig. 3A). In the medium-diameter regime ( $d \sim 1.4 \text{ to } 2 \text{ nm}$ ), M-SWNTs were selectively etched/removed over semiconducting ones. In the large-diameter regime ( $d > 2 \text{ nm}$ ), both M- and S-SWNTs were not etched by the plasma (Fig. 3A).

Etching of SWNTs in the methane plasma is attributed to hydrocarbonation, with SWNTs irreversibly etched (19) into hydrocarbon gas species as a result of reactions with neutral and positive ions of H and  $\text{CH}_3$  species in a methane plasma (20). The results above show that diameter is an important factor for the chemical reactivity of a SWNT toward hydrocarbonation. Smaller-diameter SWNTs are preferentially etched over larger ones because of the higher radius of curvature and higher strain in the C-C bonding configuration, as in other chemical reactions [e.g., oxidation (21)] of SWNTs. In the small- and large-diameter

regimes, respectively, SWNTs are either etched or unaffected without selectivity over metallicity (Fig. 3A). In the medium-diameter range, metallic tubes are selectively etched over semiconducting ones (Fig. 3A). This is consistent with first-principles calculations (22, 23) that the formation energies of same-diameter S-SWNTs are lower than M-SWNTs because of the electronic energy gain resulting from the band gap opening (22) and the higher chemical reactivity of M-SWNTs due to more abundant

delocalized electronic states (23). The difference diminishes for SWNTs with large diameters (22), consistent with reduced chemical etching selectivity seen here for large tubes. It is notable that the window of selective M-SWNT etching is small and exploitable only with methane plasma treatment. With pure hydrogen-generated plasma, we observed diameter-dependent etching (19) but failed to etch M-SWNT selectively and enrich depletable nanotube FETs. Pure hydrogen

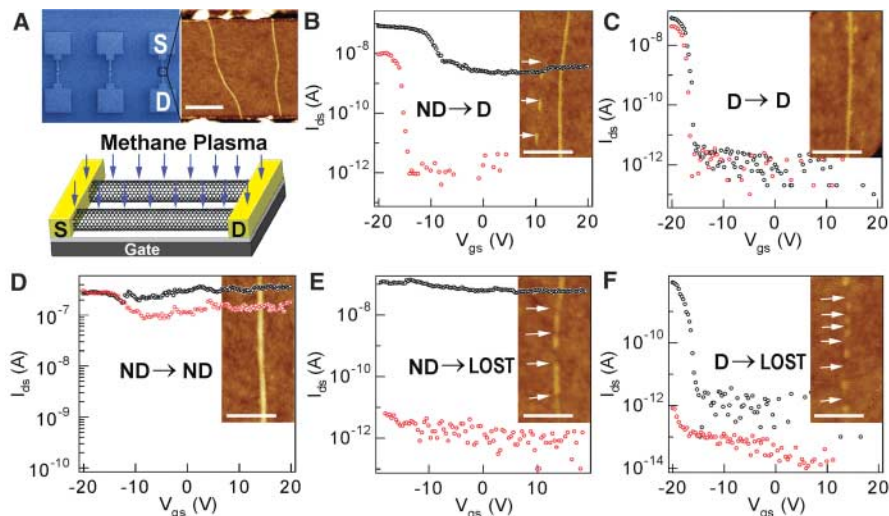


**Fig. 1.** Selective etching of metallic carbon nanotubes from the gas phase. (A) (Top) A scanning electron microscope (SEM) image of an array of few-tube (0 to 3) devices and an AFM image of two SWNTs bridging S-D electrodes. (Bottom) Schematic of the methane plasma treatment step [see (18) for details]. (B to F) Current ( $I_{ds}$ ) versus gate voltage ( $V_{gs}$ ) characteristics ( $V_{ds} = 10 \text{ mV}$ ) showing five different evolutions before (black) and after (red) the plasma and annealing treatment. Inset in each graph is an AFM image showing nanotubes in each device recorded after the treatment. White arrows highlight etched tubes in the devices. Scale bars, 100 nm.

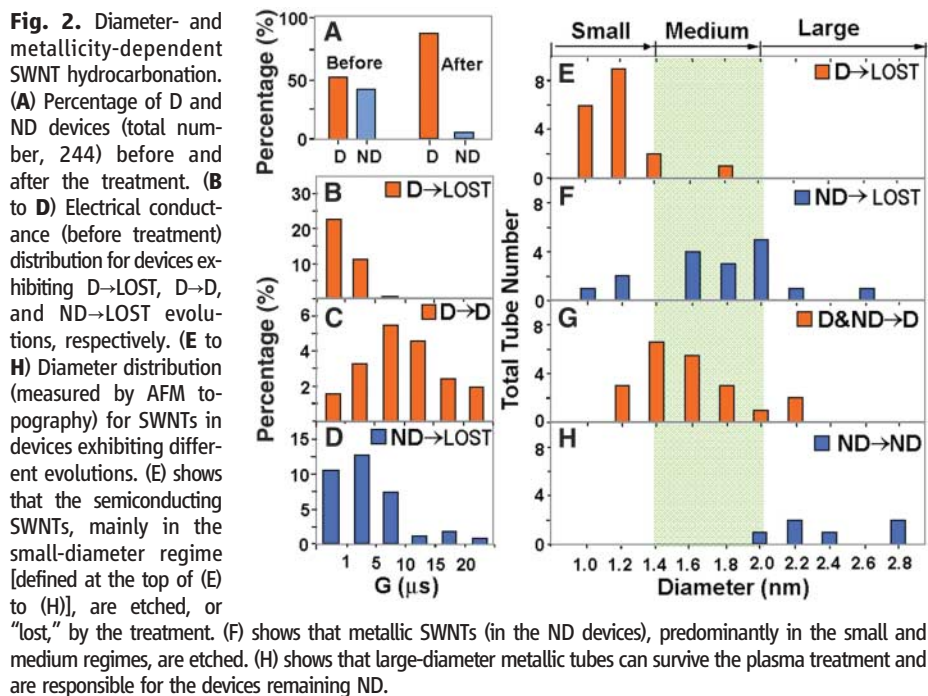


**Fig. 2.** Diameter- and metallicity-dependent SWNT hydrocarbonation. (A) Percentage of D and ND devices (total number, 244) before and after the treatment. (B to H) Electrical conductance (before treatment) distribution for devices exhibiting D $\rightarrow$ LOST, D $\rightarrow$ D, and ND $\rightarrow$ LOST evolutions, respectively. (E to H) Diameter distribution (measured by AFM topography) for SWNTs in devices exhibiting different evolutions. (E) shows that the semiconducting SWNTs, mainly in the small-diameter regime [defined at the top of (E) to (H)], are etched, or “lost,” by the treatment. (F) shows that metallic SWNTs (in the ND devices), predominantly in the small and medium regimes, are etched. (H) shows that large-diameter metallic tubes can survive the plasma treatment and are responsible for the devices remaining ND.

plasma appeared too reactive to control experimentally, causing nondiscriminating etching effects.

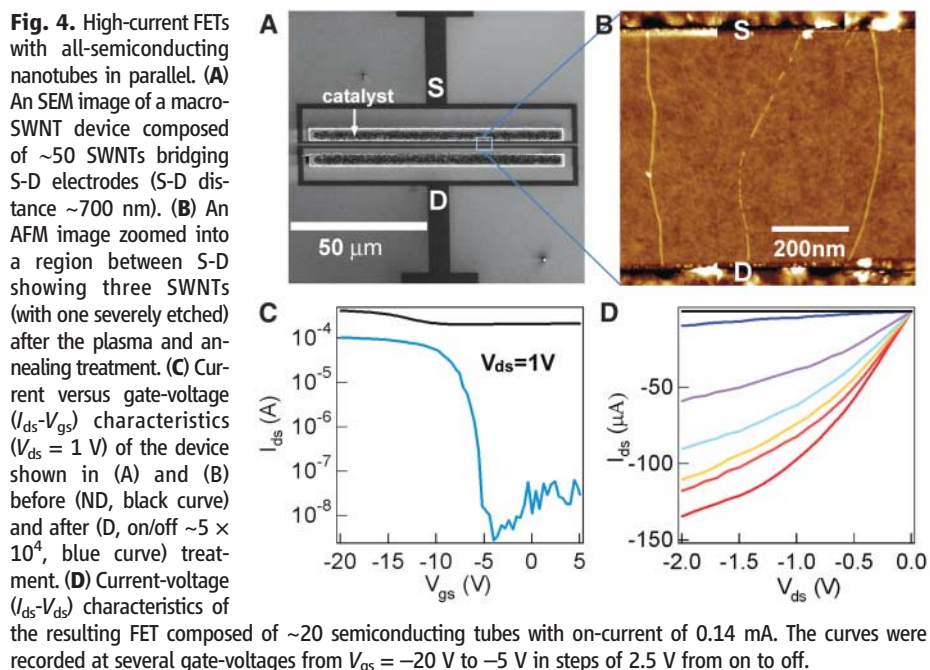
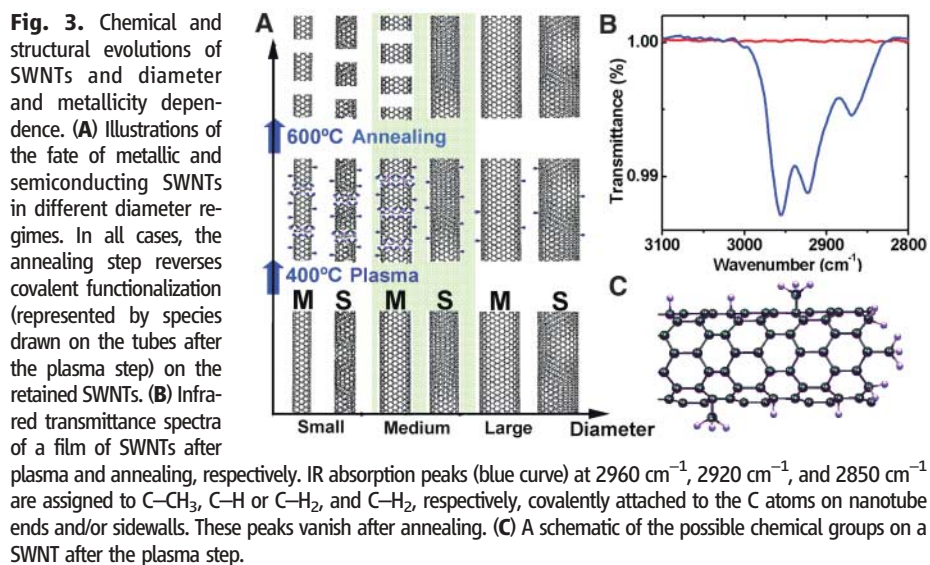
Covalent chemical groups on nanotubes cause  $sp^3$  hybridization (tetrahedral bonding) and degrade electrical properties and device performance. We carried out infrared (IR) spectroscopic experiments with ensembles of SWNTs to check the chemical effects of our treatment. After the 400°C methane plasma treatment step, we detected IR vibrational modes that can be assigned to covalent C-H<sub>x</sub> groups (24) on nanotubes at either sidewalls or ends (Fig. 3, B and C). These species vanished upon 600°C vacuum annealing, indicating the elimination of covalently bound groups through demethylation and dehydrogenation. Thus, the

600°C annealing step ensured that the semiconducting SWNTs in the final FET devices were free of covalently attached species. This is further evidenced by retained electrical properties of nonetched S-SWNTs (18) (Fig. 1C and fig. S2).

Next, we showed that our method is reliable and can provide a 100% yield of semiconductors in an ensemble of SWNTs. For demonstration of FETs with large numbers of S-SWNTs in parallel, we fabricated arrays of micro devices (Fig. 4, A and B) with 40 to 50 CVD-grown SWNTs bridging S-D electrodes (channel length  $\sim 700$  nm) on SiO<sub>2</sub>(67 nm)/Si substrates. The catalyst islands and electrodes substrates were designed to be  $\sim 100$  to 200  $\mu\text{m}$  for growth and for wiring up large numbers of

tubes (Fig. 4A). We optimized CVD growth by lowering the growth temperature to 750°C to produce SWNTs with diameters predominantly in the 1- to 1.8-nm range. As-made devices were all nondepletable, with negligible on/off ratios due to metallic tubes (Fig. 4C, black curve). After our treatment steps, all devices exhibited improved on/off ratios, affording FETs with on/off of  $10^4$  to  $10^5$  at  $V_{ds} = 1$  V (Fig. 4C, blue curve) and high on-currents ( $I_{ds} \sim 140$   $\mu\text{A}$  at  $V_{ds} = 2$  V) (Fig. 4D). AFM revealed  $\sim 20$  intact semiconducting SWNTs in parallel in such devices (together with residues of etched M-SWNTs) (Fig. 4B) without any metallic short (a single M-SWNT mixed with  $\sim 20$  S-SWNTs would degrade on/off to  $\sim 10$ ). The properties of our macro-FETs (on-current,  $\sim 5$  to 7  $\mu\text{A}$  per tube) are comparable to the best  $\sim 700$ -nm-long channel devices of similar diameter ( $\sim 1.4$  nm) S-SWNTs in as-grown forms (16). Multitube FETs were reproducibly obtained with large numbers of devices (fig. S3) (18), providing strong evidence for the effectiveness of our method.

Our present work focuses on only one of the ingredients needed for eventual manufacturing of nanotube electronics. Other important elements are still required, including assembly of SWNTs in a closely packed manner on wafer substrates. Hydrocarbonation etching can then be used to permanently remove metallic tubes from the wafers, which will then reduce the packing between the retained S-SWNTs. This reduced packing will be acceptable and could favor electrostatics gate control over SWNTs in the assembly (25). Our gas-phase reaction can be easily integrated into fabrication processes and is advantageous over wet chemical treatments, as the latter tend to involve excessively short SWNTs caused by sonication, too-small-diameter tubes in the starting materials, or covalent groups remaining on the SWNTs. The starting nanotube materials for future electronics should have diameters of 1.3 to 1.6 nm, beyond which the nanotubes will be too small for high performance or too large to attain pure semiconductors. An important benefit of narrow-diameter distribution ( $\sim 1.5$  nm) is that fewer SWNTs (up to about one-third, which is the metallic fraction) will need to be etched or sacrificed. Thus, with suitable starting materials and advances in assembly and selective-etching chemistry, a road map can be envisioned for manufacturable nanotube electronics.



#### References and Notes

1. C. Dekker, *Phys. Today* **52**, 22 (1999).
2. P. L. McEuen, M. S. Fuhrer, H. K. Park, *IEEE Trans. Nanotechnology* **1**, 78 (2002).
3. A. Javey, J. Guo, Q. Wang, M. Lundstrom, H. J. Dai, *Nature* **424**, 654 (2003).
4. A. Javey *et al.*, *Nano Lett.* **4**, 1319 (2004).
5. Y. M. Lin *et al.*, *IEEE Elec. Dev. Lett.* **26**, 823 (2005).
6. J. Appenzeller, Y. M. Lin, J. Knoch, Z. H. Chen, P. Avouris, *IEEE Trans. Elec. Dev.* **52**, 2568 (2005).

7. S. M. Bachilo *et al.*, *J. Am. Chem. Soc.* **125**, 11186 (2003).  
 8. Y. M. Li *et al.*, *Nano Lett.* **4**, 317 (2004).  
 9. P. Collins, M. Arnold, P. Avouris, *Science* **292**, 706 (2001).  
 10. R. Seidel *et al.*, *Nano Lett.* **4**, 831 (2004).  
 11. D. Chattopadhyay, L. Galeska, F. Papadimitrakopoulos, *J. Am. Chem. Soc.* **125**, 3370 (2003).  
 12. M. Zheng *et al.*, *Science* **302**, 1545 (2003).  
 13. M. S. Strano *et al.*, *Science* **301**, 1519 (2003).  
 14. K. Balasubramanian, R. Sordan, M. Burghard, K. A. Kern, *Nano Lett.* **4**, 827 (2004).  
 15. L. An, Q. A. Fu, C. G. Lu, J. Liu, *J. Am. Chem. Soc.* **126**, 10520 (2004).  
 16. W. Kim *et al.*, *Appl. Phys. Lett.* **87**, 1 (2005).  
 17. J. Kong, H. Soh, A. Cassell, C. F. Quate, H. Dai, *Nature* **395**, 878 (1998).  
 18. Materials and methods are available as supporting materials on *Science* Online.  
 19. G. Y. Zhang *et al.*, *J. Am. Chem. Soc.* **128**, 6026 (2006).  
 20. G. Drabner, A. Poppe, H. Budzikiewicz, *Int. J. Mass Spectrom. Ion Process.* **97**, 1 (1990).  
 21. W. Zhou *et al.*, *Chem. Phys. Lett.* **350**, 6 (2001).  
 22. Y. Li *et al.*, *J. Phys. Chem. B* **109**, 6968 (2005).  
 23. H. Park, J. Zhao, J. P. Lu, *Nanotechnology* **16**, 635 (2005).  
 24. T. Heitz, B. Drevillon, C. Godet, J. E. Bouree, *Phys. Rev. B* **58**, 13957 (1998).  
 25. J. Guo, S. Goasguen, M. Lundstrom, S. Datta, *Appl. Phys. Lett.* **81**, 1486 (2002).  
 26. We thank Intel and MARCO Center for Materials, Structures, and Devices for support of this work.

### Supporting Online Material

www.sciencemag.org/cgi/content/full/314/5801/974

DC1

Materials and Methods

Figs. S1 to S3

11 August 2006; accepted 3 October 2006

10.1126/science.1133781

# Metamaterial Electromagnetic Cloak at Microwave Frequencies

D. Schurig,<sup>1</sup> J. J. Mock,<sup>1</sup> B. J. Justice,<sup>1</sup> S. A. Cummer,<sup>1</sup> J. B. Pendry,<sup>2</sup> A. F. Starr,<sup>3</sup> D. R. Smith<sup>1\*</sup>

A recently published theory has suggested that a cloak of invisibility is in principle possible, at least over a narrow frequency band. We describe here the first practical realization of such a cloak; in our demonstration, a copper cylinder was “hidden” inside a cloak constructed according to the previous theoretical prescription. The cloak was constructed with the use of artificially structured metamaterials, designed for operation over a band of microwave frequencies. The cloak decreased scattering from the hidden object while at the same time reducing its shadow, so that the cloak and object combined began to resemble empty space.

A new approach to the design of electromagnetic structures has recently been proposed, in which the paths of electromagnetic waves are controlled within a material by introducing a prescribed spatial variation in the constitutive parameters (*1, 2*). The recipe for determining this variation, based on coordinate transformations (*3*), enables us to arrive at structures that would be otherwise difficult to conceive, opening up the new field of transformation optics (*4, 5*).

One possible application of transformation optics and media is that of electromagnetic cloaking, in which a material is used to render a volume effectively invisible to incident radiation. The design process for the cloak involves a coordinate transformation that squeezes space from a volume into a shell surrounding the concealment volume. Maxwell’s equations are form-invariant to coordinate transformations, so that only the components of the permittivity tensor  $\epsilon$  and the permeability tensor  $\mu$  are affected by the transformation (*5*), becoming both spatially varying and anisotropic. By implementing these complex material properties, the concealed volume plus the cloak appear to have the properties of free space when viewed externally. The cloak thus

neither scatters waves nor imparts a shadow in the transmitted field, either of which would enable the cloak to be detected. Other approaches to invisibility either rely on the reduction of backscatter or make use of a resonance in which the properties of the cloaked object and the cloak itself must be carefully matched (*6, 7*).

It might be of concern that we are able to achieve two different solutions to Maxwell’s equations that both have, in principle, the exact same field distributions on a surface enclosing the region of interest. Indeed, the uniqueness theorem would suggest that these two solutions would be required to have the exact same medium within the surface. The uniqueness theorem, however, applies only to isotropic media (*8, 9*); the required media that result from our coordinate transformations are generally anisotropic. Such media have been shown to support sets of distinct solutions having identical boundary conditions (*10, 11*).

The effectiveness of a transformation-based cloak design was first confirmed computationally in the geometric optic limit (*1, 5*) and then in full-wave finite-element simulations (*12*). Advances in the development of metamaterials (*13*), especially with respect to gradient index lenses (*14, 15*), have made the physical realization of the specified complex material properties feasible. We implemented a two-dimensional (2D) cloak because its fabrication and measurement requirements were simpler than those of a 3D cloak. Recently, we have demonstrated the capability of obtaining de-

tailed spatial maps of the amplitude and phase of the electric field distribution internal to 2D negative-index metamaterial samples at microwave frequencies (*16*). Using this measurement technique, we confirmed the performance of our cloak by comparing our measured field maps to simulations.

In both the cloaking simulations and the measurements presented here, the object being cloaked is a conducting cylinder at the inner radius of the cloak; this is the largest and most strongly scattering object that can be concealed in a cloak of cylindrical geometry.

For the cloak design, we start with a coordinate transformation that compresses space from the cylindrical region  $0 < r < b$  into the annular region  $a < r' < b$ , where  $r$  and  $r'$  are the radial coordinates in the original and transformed system, respectively,  $a$  is the cloak inner radius, and  $b$  is the cloak outer radius. A simple transformation that accomplishes this goal is

$$r' = \frac{b-a}{b}r + a \quad \theta' = \theta \quad z' = z \quad (1)$$

where  $\theta$  and  $z$  are the angular and vertical coordinates in the original system, and  $\theta'$  and  $z'$  are the angular and vertical coordinates in the transformed system. This transformation leads to the following expression for the permittivity and permeability tensor components

$$\epsilon_r = \mu_r = \frac{r-a}{r} \quad \epsilon_\theta = \mu_\theta = \frac{r}{r-a}$$

$$\epsilon_z = \mu_z = \left(\frac{b}{b-a}\right)^2 \frac{r-a}{r} \quad (2)$$

Equation 2 shows that all of the tensor components have gradients as a function of radius, implying a very complicated metamaterial design. However, because of the nature of the experimental apparatus, in which the electric field is polarized along the  $z$  axis (cylinder axis), we benefit from a substantial simplification in that only  $\epsilon_z$ ,  $\mu_r$ , and  $\mu_\theta$  are relevant. Moreover, if we wish to primarily demonstrate the wave trajectory inside the cloak, which is solely determined by the dispersion relation, we gain even more flexibility in choosing the functional forms for the electromagnetic ma-

<sup>1</sup>Department of Electrical and Computer Engineering, Duke University, Box 90291, Durham, NC 27708, USA. <sup>2</sup>Department of Physics, The Blackett Laboratory, Imperial College, London SW7 2AZ, UK. <sup>3</sup>SensorMetrix, 5695 Pacific Center Boulevard, San Diego, CA 92121, USA.

\*To whom correspondence should be addressed. E-mail: drsmith@ee.duke.edu



## Supporting Online Material for

### **Selective Etching of Metallic Carbon Nanotubes by Gas-Phase Reaction for Scalable Electronics**

Guangyu Zhang, Pengfei Qi, Xinran Wang, Yuerui Lu, Xiaolin Li, Ryan Tu,  
Sarunya Bangsaruntip, David Mann, Li Zhang, Hongjie Dai\*

\*To whom correspondence should be addressed. E-mail: hdai@stanford.edu

Published 17 November 2006, *Science* **314**, 974 (2006)  
DOI: 10.1126/science.1133781

#### **This PDF file includes:**

Materials and Methods  
Figs. S1 to S3

**Supporting Online Material For:****Selective Etching of Metallic Carbon Nanotubes by Gas Phase Reaction for Scalable Electronics**

Guangyu Zhang, Pengfei Qi, Xinran Wang, Yuerui Lu, Xiaolin Li, Ryan Tu, Sarunya Bangsaruntip, David Mann, Li Zhang and Hongjie Dai\*

\* To whom correspondences should be addressed. E-mail: hdai@stanford.edu

**This file includes:**

Materials and Methods  
Figs. S1, S2 and S3

**(1) Materials and Methods:****(1.1) CVD growth of SWNTs for ‘few-tube’ devices with nanotubes in the diameter range of 1-2.8nm.**

For few-tube-devices, arrays of relatively small  $5 \times 5 \mu\text{m}$  catalyst island pairs (nominally  $\sim 1 \text{ \AA}$  cobalt film whose thickness was monitored by quartz crystal thickness monitor;  $10 \mu\text{m}$  spacing to each other.) were patterned on  $\text{SiO}_2/\text{Si}$ . The substrates with patterned catalyst arrays were calcined in air at  $500^\circ\text{C}$  for 30 minutes to burn any photo resist (PMMA) residue used in the patterning step and then heated up in hydrogen to  $800^\circ\text{C}$ . Alcohol CVD growth was carried out using a gas mixture of Ar (200sccm) and ethanol (300sccm) vapor (generated from a alcohol bubbler maintained at  $-8.9^\circ\text{C}$  by passing through a 300sccm forming gas). The growth temperature was  $800^\circ\text{C}$  and the total CVD lasted for 10 minutes. The  $\sim 1 \text{ \AA}$  Co film catalyst and  $800^\circ\text{C}$  produced nanotubes with diameters in the 1-3nm range as revealed by AFM measurements of about 100 nanotubes.

**(1.2) CVD growth of SWNTs for many-tube ‘macro’ devices with nanotubes predominantly in the diameter range of  $\sim 1-1.8 \text{ nm}$ .**

For macro-devices comprised of large number of SWNTs in each device, the catalyst island pairs were  $100 \mu\text{m}$  wide with  $5 \mu\text{m}$  spacing to each other. The Co catalyst film

thickness was  $\sim 0.5\text{\AA}$ . SWNTs were grown from these catalyst patterns by the alcohol CVD mentioned above except that the growth temperature was lowered to  $750^\circ\text{C}$ . The thinner Co film and lower growth temperature afforded SWNTs predominantly in the 1-1.8nm range.

### **(1.3.) Device fabrication.**

After CVD growth, microfabrication techniques were used to pattern source-drain S-D metal electrode arrays to contact SWNTs grown from the catalyst islands. The channel lengths (S-D distance) were  $\sim 300\text{ nm}$  and  $\sim 700\text{ nm}$  for few-tube devices macro devices respectively. We chose Ti/Au (1nm/20nm) as contact metal in the current work since our treatment method involved a  $600^\circ\text{C}$  annealing step. Typically, we obtained 40-50% of connections for the 98 few-tube device arrays on each chip, and the number of tubes in each device was 1 to 3. For macro-devices, we obtained 100% connections due to the large number of SWNTs (30-50) grown from the wide catalyst pattern.

### **(1.4) Details of the methane plasma and annealing treatment method.**

Fig. S1 shows a schematic drawing of the setup used for our high temperature methane plasma and annealing treatment of SWNTs. The tube-furnace was  $\sim 5$ -inch in diameter capable of processing 4-inch wafers. Inductively coupled plasma was generated at the entrance of the furnace using an RF (13.56 MHz) coil. The three-zone furnace was used to heat up samples to a desired temperature. The sample was placed at the center of the furnace and away from the RF coil region to avoid direct exposure to the as-generated plasma. The plasma was generated outside the furnace and carried downstream to reach the SWNT sample.

Our high temperature methane plasma treatment condition used the following experimental parameters: temperature at sample =  $400^\circ\text{C}$ , plasma power 50W, pressure in the tube furnace  $\sim 0.35\text{ torr}$  maintained by flowing a mixture of methane and Ar (80% methane) at 320 sccm and vacuum pumping. For few-tubes devices, the plasma treatment time was 10 min. For the macro-devices, the plasma treatment time was increased to 20 min. Immediately following the plasma treatment, the samples were heated in vacuum (with a low background pressure of molecular hydrogen) to  $600^\circ\text{C}$  for 20 minutes before

cooled down to room temperature. Note that prior to the plasma treatment, the as-made SWNT devices on each chip were annealed in vacuum at 600°C for 20 minutes to remove potential organic residues (e.g., photo resists).

### **(1.5) Infrared experiments for investigation of chemical groups on nanotubes**

In order to maximize IR signal and glean the vibrational modes of any chemical species on SWNTs by FTIR experiments, we employed vertically aligned SWNT films comprised of high density of SWNTs on silicon oxide substrates (for details of samples see: Zhang, G. Y., Mann, D., Zhang, L., Javey, A., Li, Y. M., Yenilmenz, E., Wang, Q., McVittie, J., Nishi, Y., Gibbons, J., Dai, H. *PNAS* **102**, 16141-16145 (2005).). These films were first annealed at 700°C to remove any absorbed species. The IR spectra of the films were then recorded and used as background. IR spectra were recorded again after the high temperature plasma treatment and 600 °C annealing steps respectively and plotted (in Fig. 3B of main text) after subtracting the back-ground spectra recorded before the plasma treatment.

IR spectra were recorded with a Vertex 70 IR spectrometer (Bruker) equipped with a DuraSampl *IR* sampling system that uses a diamond sampling interface operated in a horizontal ATR (attenuated total reflection) configuration. The diamond is the effective ATR crystal that affords multiple reflections at the sample surface. During IR measurements, the vertical SWNT films were pressed by the diamond tip (1mm in radius) with a force of 20 lb.

## **2. Supporting Figures:**

### **(2.1) Experimental setup for methane plasma and annealing treatment of SWNTs.**

Fig. S1 shows a schematic drawing of the setup used for our high temperature methane plasma and annealing treatment of SWNTs.

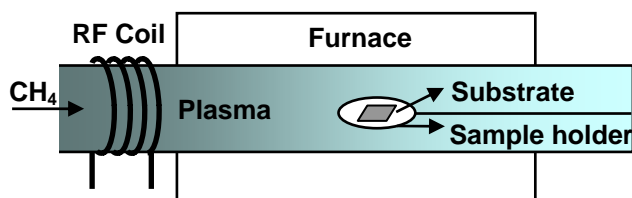
### **(2.2) Electrical properties of the retained semiconducting SWNTs are largely preserved.**

Fig. S2 shows two examples (in addition to Fig.1C of main text) of retained S-SWNT

FETs (for few-tube devices) through the plasma and annealing treatment steps. The electrical conductance of the S-SWNTs exhibit decreases (blue curve) after the plasma step attributed to side-wall hydrogenation, and largely recover (red curve) to the original level (black curve) after 600°C annealing.

**(2.3) More examples of our high current macro-FETs composed of multiple all-semiconducting SWNTs.**

Fig. S3 in next page shows more examples of multiple S-SWNT FETs with high on-currents ( $\sim 100\mu\text{A}$ ) and on/off ratios ( $10^5$ - $10^6$ ) obtained on the same chip as the device shown in Fig. 4. These devices illustrate the reproducibility of our method in obtaining such devices. As-made devices were all ND (non-depletable) with negligible on/off ratios due to metallic tubes. After the treatment, all devices exhibited drastically improved on/off ratios and about 1/3 of the devices become depletable with on/off ratio higher than  $10^3$ . AFM revealed  $\sim 20$  intact semiconducting SWNTs in such devices. There are a small percentage of macro-devices failed to exhibit on/off  $>10^4$  due to the existence of occasional large diameter SWNTs in the devices by our CVD synthesis. Growth of SWNTs with diameters exclusively below the 1.8nm limit will ensure the production of high performance of many-tube FETs with 100% efficiency.



**Figure S1:** A schematic drawing of our experimental setup used to carry out methane plasma etching of SWNT samples and subsequent annealing.

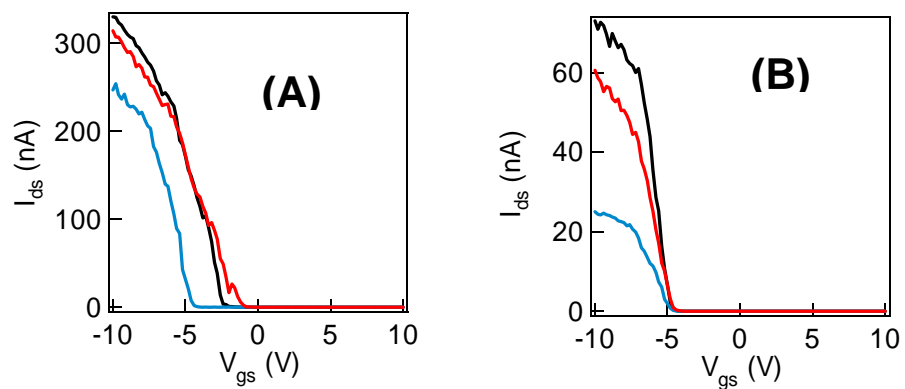


**Figure S2.** Transfer characteristics (at  $V_{ds}=10$  mV) of two CVD grown S-SWNT devices in as-fabricated form (black), after plasma treatment (blue) and after annealing (red).

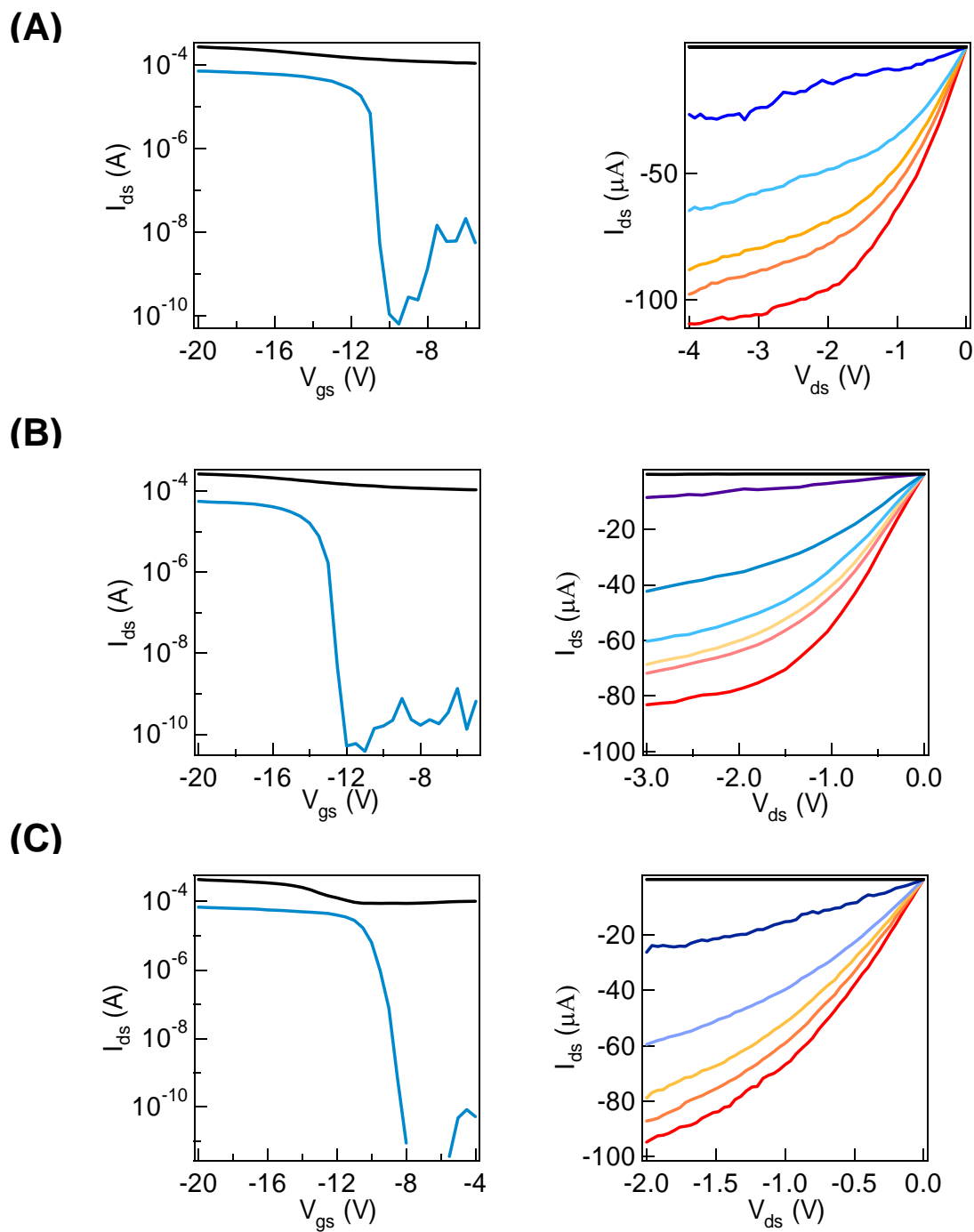


**Figure S3.** A-C three different multi-tube FETs. Left panel: current vs. gate characteristics (under 1V bias) before (black) and after (blue) treatments. Right panel: current-voltage curves of the resulting FETs under various gate-voltages from  $V_{gs} = -20$  V to  $-10$  V in steps of 2V from on to off.